applied sciences

MDPI

Article

The Effect of the Vertical Component of the Earthquake on a Regular Masonry Wall

Guido Camata, Alice Di Primio *, Vincenzo Sepe and Cristina Cantagallo

Department of Engineering and Geology, University of Chieti-Pescara G. D'Annunzio, Viale Pindaro 42, 65127 Pescara, Italy

* Correspondence: alice.diprimio@unich.it

Abstract: The effect of the vertical component of earthquakes on the structural behaviour of unreinforced masonry (URM) walls is usually not considered by technical codes for ordinary buildings. Recent scientific literature, however, indicates that the earthquake vertical component may play a significant role in the crack pattern of URM walls and their collapse. This paper investigates the effect of the vertical seismic component on the capacity and damage scenario for a two-story regular URM wall, described with a detailed micro-modelling approach. Pushover and nonlinear time history analyses are carried out with and without the vertical component and under different dead loads representative of typical stress states for URM structures. The inter-story drift and roof drift ratios are introduced as Engineering Demand Parameters (EDPs), and their correlation with the Ground Motion Parameters (GMPs) of the horizontal and vertical components is discussed. The results show a very good correlation between the seismic demand and the GMPs of the vertical component, demonstrating the influence of the vertical component on the global seismic response. Moreover, the study shows that the influence of the vertical component increases with the vertical load applied to the structure, which indicates that the vertical ground motion component cannot be a priori neglected for URM walls when moderate to large vertical GMPs are expected.

Keywords: masonry structures; URM walls; earthquake vertical component; micro-modelling; nonlinear static analysis; nonlinear time history analysis

check for updates

Citation: Camata, G.; Di Primio, A.; Sepe, V.; Cantagallo, C. The Effect of the Vertical Component of the Earthquake on a Regular Masonry Wall. *Appl. Sci.* **2023**, *13*, 2459. https://doi.org/10.3390/app13042459

Academic Editor: Arcady Dyskin

Received: 3 January 2023
Revised: 9 February 2023
Accepted: 10 February 2023
Published: 14 February 2023

1. Introduction

Following the indications of Eurocode 8 EN1998-1 §4.3.3.5.2 [1] and EN1998-3 §4.4.7 [2], the vertical component of the seismic action is considered only when the Peak Ground Acceleration (PGA) of the ground motion is greater than $0.25\times g$ and in the following cases:

- for horizontal or nearly horizontal structural members spanning 20 m or more;
- for horizontal or nearly horizontal cantilever components longer than 5 m;
- for horizontal or nearly horizontal pre-stressed components;
- for beams supporting columns;
- in base-isolated structures.

In the published literature, the relationship between vertical and horizontal response spectra of the free field ground motion recorded is studied to show the importance of the vertical component of earthquake ground motion in seismic analysis. Pioneering studies have shown that the relationship between vertical and horizontal (V/H) response spectra is highly dependent on the period and site distance from the seismic source [3–6]. The literature shows that the vertical component of the earthquake plays a fundamental role in defining the crack pattern of the elements and their collapse. Different papers studied the two main shocks of the 2016 Central Italy seismic sequence. Liberatore et al. [7] compared the Interferometric Synthetic Aperture Radar (InSAR) findings of the 2016 Amatrice earthquake with the macro-seismic data, highlighting how, in masonry structures with small cohesion, the vertical component increases masonry vulnerability. This result was confirmed in other studies that analysed the 2012 Emilia Romagna earthquake [8–10]. The analysis of the crack pattern of some structures, e.g., the clock tower in Emilia Romagna [11], confirmed that, for low-strength masonry structures, the influence of the vertical component of the earthquake leads to severe damage of the structures or even to their collapse.

Recent papers on historic masonry structures studied the effects of the earthquake vertical component considering different conditions: the characteristics of the seismic event affecting the area [12–16], the distance from the epicentre [16], and the type of structure [17,18]. In Kallioras et al. [19], the damage potential of vertical accelerations was investigated through a series of multidirectional shake table tests on full-scale structures under simulated near-source ground motions of increasing intensity. The experiments comprised three nominally identical building specimens subjected to the principal horizontal component alone, the horizontal component combined with the vertical one, and the full three-component ground motion. In Chieffo et al. [20], a FEM model of the Banloc castle, a historical building in Romania, was investigated in the nonlinear dynamic field to evaluate the influence of the vertical seismic component in terms of displacement stress and crack pattern, accounting for only the horizontal component and the horizontal and vertical components. In Brunelli et al. [21], to simulate the seismic performance of the "Pietro Capuzi" school in Visso, the Marche Region (Italy), under a series of seismic motion events similar to those produced by the 2016–2017 Central Italy earthquake, the sequence of acceleration time histories recorded along both horizontal directions X and Y at the base and the vertical component were applied to nonlinear EF models with both fixed and compliant bases.

This paper aims to evaluate the influence of the vertical component of the earthquake on a 2D wall implemented in the OpenSees framework with STKO analysis software [22] using a micro-modelling approach.

The choice of this modelling approach is made considering the type of analysis to be carried out and the case study. Following a bibliographic study, it is possible to affirm that the main advantage of this type of modelling is the accuracy in predicting the failure load and the collapse mechanism, as demonstrated in [23,24]. It has been shown that the micro-model is able to obtain results of very similar collapse mechanisms on unreinforced masonry structures.

Section 3 of the paper describes the case–study structure, with the geometric characterization, mechanical properties, and calibration of the structural micro-model. Section 4 shows the results of Pushover (PO) analyses carried out considering different vertical loading conditions, representing typical conditions for masonry structures. Nonlinear Time History Analyses (NTHAs) carried out by subjecting the structure to three different earthquakes and different vertical loads are described in Section 5, where the selected ground motion records, the results of the analyses, and the correlations between the selected Engineering Demand Parameters (EDPs) and the Ground Motion Parameters (GMPs) are described. In Section 6, the conclusions are drawn.

2. Numerical Formulation

The model used in this work is an extension of the plastic damage model developed by Petracca et al. [25] and presented in Petracca et al. [26].

The model is based on continuum damage mechanics and uses a mixed implicit integration scheme.

The adopted model is an orthotropic model of pure tension/compression damage (d^+/d^-) based on the continuous model to accurately reproduce the nonlinear shear response of masonry walls. Failure surfaces are defined through two scalar quantities calculated using Equations (1) and (2):

$$\tau^- = H(-\overline{\sigma}_{\min})\left[\frac{1}{1-\alpha}\left(\alpha\overline{I}_1 + \sqrt{3\overline{J}_2} + k_1\beta\langle\overline{\sigma}_{\max}\rangle\right)\right] \tag{1}$$

$$\tau^{+} = H(\overline{\sigma}_{\max})\left[\frac{1}{1-\alpha}\left(\alpha\overline{I}_1 + \sqrt{3\overline{J}_2} + \beta\langle\overline{\sigma}_{\max}\rangle\right)\frac{\sigma_t}{\sigma_p}\right] \quad (2)$$

where τ^{-} represents the equivalent compression stress, τ^{+} represents the equivalent tensile stress, $\overline{\sigma}_{\max}$ represents the primary effective stress, σ_t represents the tensile strength of the units or mortar joints, σ_p represents the peak compressive strength of the units or mortar joints, I_1 is the first invariant of the effective stress tensor, J_2 is the second invariant of the effective deviatoric stress tensor, and k_1 is the ratio between the biaxial and uniaxial compressive strengths.

Equivalent stresses and damage evolution in tension and compression are defined by uniaxial stress-strain laws. The uniaxial stress laws are defined as shown in Figure 1 and are comprised of two parts: a linear part [(0; 0)—(ε_0; σ_t)] with σ_t equal to the stress resistance of the unit or mortar joints and ε_0 equal to the corresponding deformation at σ_t and of a softening branch that depends on the tensile fracture energy G_t and the characteristic length of the finite element l_{dis}.

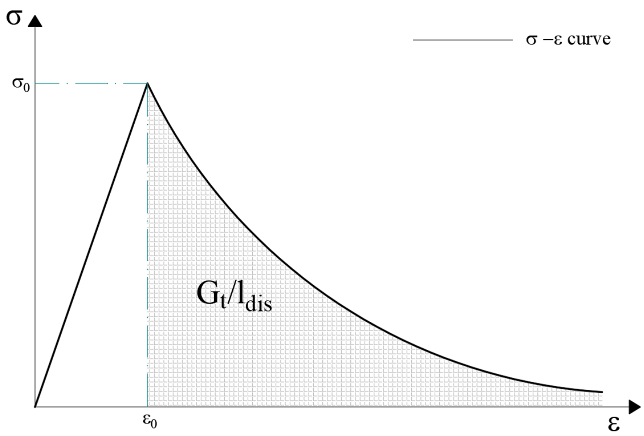

Figure 1. Uniaxial stress laws.

The uniaxial compression law is defined as in Figure 2 and is characterized by five parts: a linear part [(0; 0)—(ε_0; σ_0)], a hardening section [(ε_0; σ_0)—(ε_p; σ_p)], two softening parts [(ε_p; σ_p)—(ε_k; σ_k)] and [(ε_k; σ_k)—(ε_u; σ_u)], and a final residual [(ε_u; σ_u)—(+∞; σ_u)].

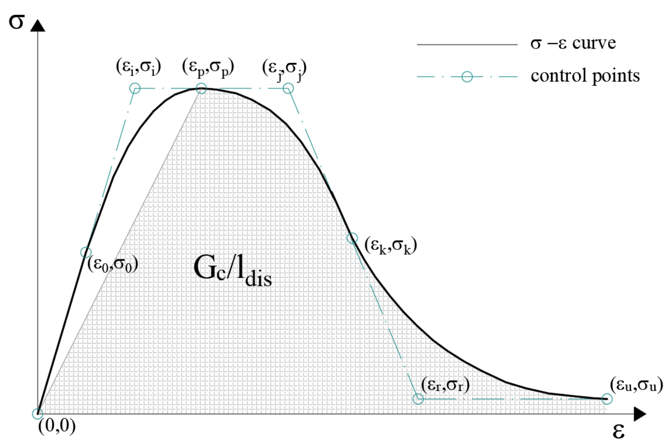

Figure 2. Uniaxial compression laws.

With:
σ_0 equal to the compression strength at the beginning of hardening;
ε_0 equal to the deformation at the beginning of hardening;
σ_p equal to the peak compression strength of the units or mortar joints;

σ_p peak deformation;
$\sigma_r = \sigma_u$ equal to residual strength;
ε_r equal to the residual deformation;
σ_u equal to the ultimate deformation;
σ_k e ε_k evaluated as intermediate control points.

All the numerical simulations shown in this work are completed using the OpenSees [27] solver, where the authors have implemented the proposed constitutive model. Pre- and post-processing are carried out with STKO software [22].

3. Case–Study Structure

This section discusses the geometrical and mechanical characteristics of the case study structure. This study considers a masonry wall with geometric characteristics similar to wall D tested in Pavia (IT) [28,29], belonging to a two-story UnReinforced Masonry (URM) building. The wall dimensions are 600 × 643 × 25 cm (length, height, and width, respectively) with four openings, two on the first floor with dimensions equal to 94 cm × 214 cm (length, height) and two on the second floor with dimensions equal to 94 cm × 124 cm (length, height), perfectly aligned with each other, as shown in Figure 3a.

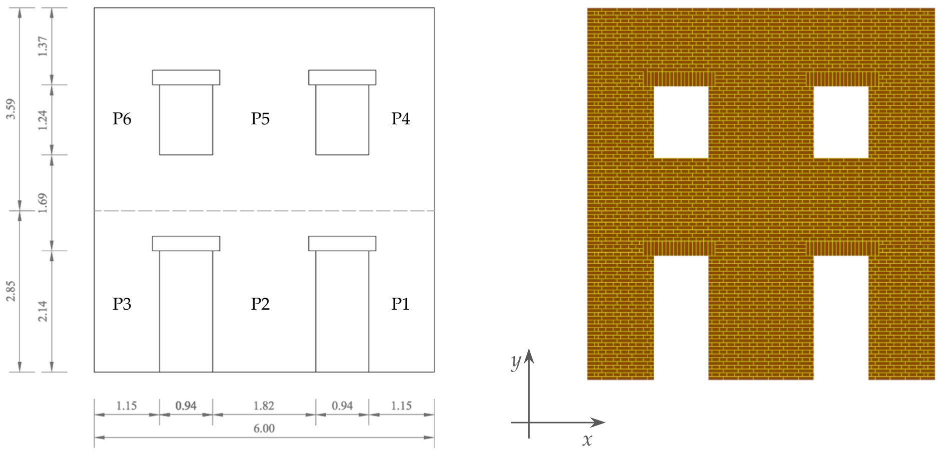

(**a**) (**b**)

Figure 3. Wall geometry: (**a**) element dimensions (m), numbering of masonry piers, and (**b**) layout of the numerical model.

Material properties are chosen to match a typical Italian historical masonry building [30]. They are characterized by solid fired-clay bricks with dimensions 25 × 12 × 5.5 cm^3 (length, thickness, and height), having a mean cubic compressive strength equal to 15 MPa and hydraulic lime mortar with a thickness of 10 mm with a compressive strength of 3.2 MPa. The brick courses are alternated to give discontinuity to the vertical mortar joints, as shown in Figure 3b.

The homogenized compressive strength of masonry is assumed to be equal to 3.2 MPa. For the micro-model, the mechanical parameters are divided between those inherent to the brick and those inherent to the mortar, as shown in Tables 1 and 2. The mortar compression strength is assumed equal to the compressive strength of the masonry, while the other parameters are assumed in agreement with the relevant scientific literature. Specifically, these would be the tensile strength of the mortar and the energy parameters of fracture of mortar and brick, which vary for calibration purposes.

Table 1. Brick material parameters.

Parameter	Unit	Value
Young's Modulus	E (N/mm^2)	6000
Poisson's ratio	ν (-)	0.2
Tensile strength	f_t (N/mm^2)	1.5
Tensile fracture energy	G_t (N/mm)	0.1
Compressive strength hardening	fc_0 (N/mm^2)	10
Compressive strength at peak	fc_p (N/mm^2)	15
Compressive strength residual	fc_r (N/mm^2)	5
Compressive deformation at peak	ε_p (-)	0.01
Compressive fracture energy	G_c (N/mm)	10

Table 2. Mortar material parameter.

Property	Symbol and Units	Value
Young's Modulus	E (N/mm^2)	350
Poisson's ratio	ν (-)	0.15
Tensile strength	f_t (N/mm^2)	0.09
Tensile fracture energy	G_t (N/mm)	0.02
Compressive strength hardening	fc_0 (N/mm^2)	1.6
Compressive strength at peak	fc_p (N/mm^2)	3.2
Compressive strength residual	fc_r (N/mm^2)	0.5
Compressive deformation at peak	ε_p (-)	0.05
Compressive fracture energy	G_c (N/mm)	70

Equal degrees of freedom in the x direction are located at each floor of the structure to prevent relative displacement between nodes in this direction. This assumption is only an approximation to represent the 2D model; it should be highlighted that the roof in the test was not a rigid diaphragm.

The analyses are developed by varying the Vertical Load (VL) representing the dead and live loads of the slabs. Three different VLs are applied to each story, i.e., 10 kN/m, 30 kN/m, and 64 kN/m. The application of the vertical loads involves an increase in the stress at the base of about 5%, 10%, and 20% respectively. The VLs were named as follows: VL-a, VL-b, and VL-c.

Figure 4 shows the shear and flexural capacities versus the applied vertical stress of the masonry piers P1 and P2 (Figure 3).

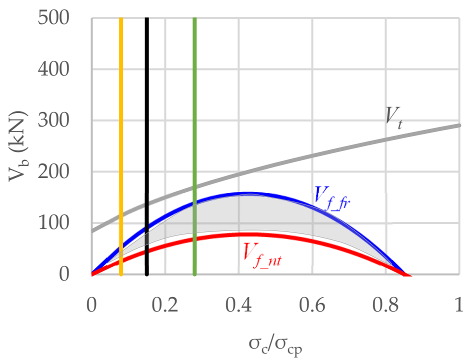

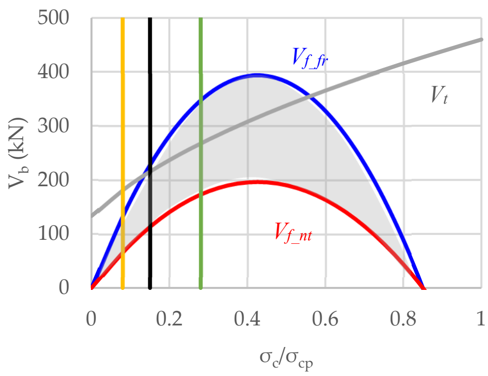

Figure 4. Resistance domains of masonry piers P1 (**left**) and P2 (**right**). Vertical lines correspond to VL-a (yellow line), VL-b (black line), and VL-c (green line). Grey lines correspond to the shear capacity V_t, and the red and blue curves refer to flexural capacities corresponding to free rotation (V_{f_fr}) or absence of rotation at the top of the panel (V_{t_nr}), respectively.

The failure criteria provided in the Italian design code [31,32] are used in this study. Thus, the in-plane flexural capacity M_u and the shear capacity V_t of the pier are calculated as indicated in Equations (3) and (4).

$$M_u = \frac{\sigma_0 l^2 t}{2}\left(1 - \frac{\sigma_0}{0.85 f_d}\right) \tag{3}$$

where M_u is the in-plane bending moment, f_d design compressive strength of masonry, 0.85 is the stress distribution coefficient, $\sigma_0 = N/(l\ t)$ the average compression stress, N is the vertical action on the pier, and l, t are the width and thickness of the pier, respectively.

$$V_t = \frac{1.5\tau_{0d} l t}{\beta}\sqrt{1 + \frac{\sigma_0}{1.5\tau_{0d}}} \tag{4}$$

where V_t is the shear capacity of the section according to the Turnšek and Čačovič [33] criterion, β is a coefficient taking into account the slenderness of the pier, and τ_{0d} is the design shear strength.

On the horizontal axis (Figure 4), vertical stress σ_c is normalized to the peak compressive strength f_{cp} (or σ_{cp}) of the masonry, while, on the vertical axis, there is the shear capacity V_b corresponding to the activation of the flexural and shear mechanisms. On each plot, the grey line refers to the shear capacity V_t controlled by the shear, while the blue and the red lines correspond to the flexural capacity V_f attained considering different constraints at the top of the panel, i.e., free rotation V_{f_fr} or the absence of rotation V_{f_nr}. The flexural capacities of Figure 4 are calculated in terms of the flexural shear V_f as the ratio between the flexural capacity M_u and the height h_0 of the point in the panel where the bending moment is equal to zero ($V_f = M_u/h_0$). The resistance domains are used to evaluate the capacity of the masonry piers analysed and the collapse mechanisms expected for different loading conditions. Vertical lines corresponding to VL-a (yellow line), VL-b (black line), and VL-c (green line) of the ratio σ_c/σ_{cp} are placed over the resistance domains to predict the range of possible resistance values. For example, for VL-c (green lines), the V_b of masonry pier P2 can vary from 160 to 340 kN.

Table 3 reports the first three linear periods of the structure studied and the corresponding mass participation ratios for each loading condition. The modal analysis shows that, for each VL, the horizontal and vertical modes are uncoupled, and the vertical response of the building is predominantly governed by the third mode of the structure.

Table 3. Vibration modes and mass participation ratios for VL-a (at left), VL-b (at centre), and VL-c (at right).

VL-a			VL-b			VL-c		
T (s)	**M_x (%)**	**M_y (%)**	**T (sec)**	**M_x (%)**	**M_y (%)**	**T (sec)**	**M_x (%)**	**M_y (%)**
0.1328	79.57	0.00	0.1888	81.75	0.00	0.2576	83.07	0.00
0.0494	13.33	0.00	0.0700	14.14	0.00	0.0947	14.47	0.00
0.0451	0.00	87.54	0.0634	0.00	89.93	0.0861	0.00	91.30

4. Pushover Analyses

This section describes the results of the Pushover (PO) analyses for the structure studied. The PO analyses are developed using the horizontal load with a uniform distribution proportional to the masses (positive and negative). The horizontal load is concentrated at the plane levels (at the node).

Figure 5 shows the PO curves. The vertical axis shows the base shear V_b, and the horizontal axis shows the Inter-story Drift Ratio (IDR) or the Roof Drift Ratio (RDR). IDR represents the ratio between the inter-story displacement and the story height, and RDR represents the ratio between the displacement on the top of the structure and its total height.

Figure 5 shows the IDR for the first story (IDR_{S1}, left), the IDR for the second story (IDR_{S2}, centre), and the RDR (right). Each plot shows the results obtained for VL-a, VL-b, and VL-c.

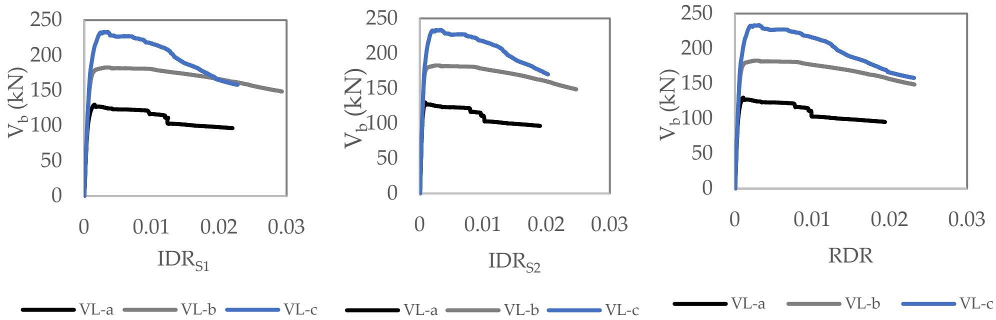

Figure 5. PO curves obtained for VL-a, VL-b, and VL-c. The three plots report the IDR of the first level (**left**), the IDR of the second level (**centre**), and the RDR (**right**) of the masonry wall.

The plots show the curves obtained for different VLs. The figure shows that the IDR_{S1} values are higher than the corresponding IDR_{S2} and RDR values. For this reason, the IDRS1 values are considered in the PO graphs below.

In the range of the vertical loads considered, which are significantly lower than the compressive strength of the masonry, a monotonic increasing trend is observed for the peak value of the PO curve as the vertical load increases.

Figure 6 reports the PO curve evaluated for VL-a at the first level of the case–study structure and the corresponding cracking pattern at 0.5% 1%, and 2% of IDR_{S1}. The first two values are representative of the shear and bending limit states suggested by the Italian technical code [31] and CNR DT 212 [34] for the frame behaviour (piers fixed to spandrels). The Italian technical code suggests a drift limit of 2% for piers that behave as cantilevers. It is used herein as an extreme upper bound of the near-collapse conditions of an unreinforced masonry (URM) wall.

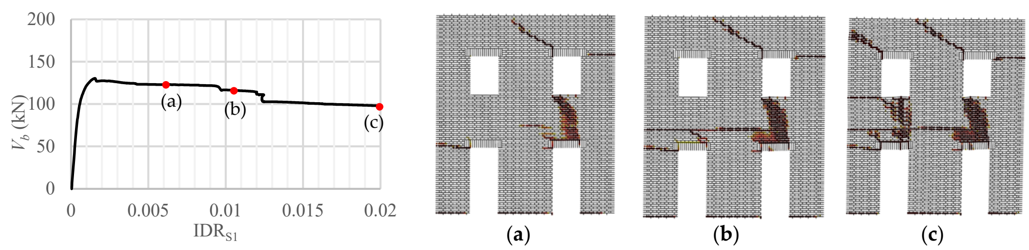

Figure 6. Cracking pattern of the masonry wall with VL-a. From left to right, damage scenarios corresponding to (**a**) 0.5%, 1% (**b**), and 2% (**c**) of IDR_{S1}.

Figure 7 shows the crack patterns corresponding to VL-a (at left), VL-b (centre), and VL-c (right) for IDR_{S1} equal to 2%. As expected, higher vertical loads correspond to a higher pier capacity, and less damage to the piers corresponds to greater damage to the spandrels.

The PO curves are described for two reasons: the first is to have a comparison between the resistant capacity of the element (V_b) obtained from the PO analysis with that obtained from the cycles of nonlinear dynamic analysis, and the second is to show how the PO curves to vary the static vertical load and then to demonstrate the reliability of the calculation models.

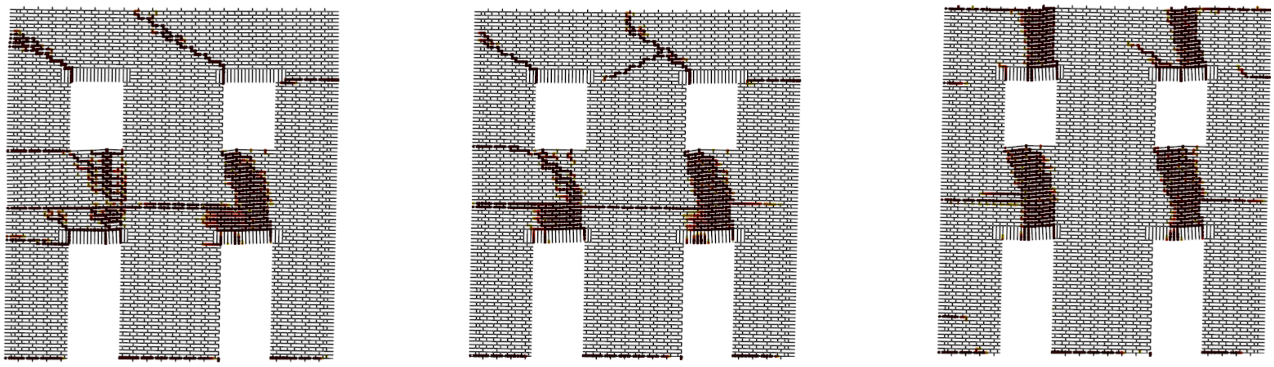

(**a**) (**b**) (**c**)

Figure 7. Crack pattern of the masonry wall corresponding to an IDR of the first level equal to 2% for (**a**) VL-a, (**b**) VL-b, and (**c**) VL-c.

5. Nonlinear Time History Analyses

This section reports the results of the NTHAs carried out using three ground motions recorded in Italy, applied to the case–study structure with and without the vertical component (V) of the seismic acceleration. The nonlinear model uses 5% damping (at the first and third mode frequencies) with full initial stiffness.

Two global Engineering Demand Parameters (EDPs) are considered for the NTHAs [35]: the IDR and the RDR.

5.1. Ground Motion Record Selection

The NTHAs performed for the case–study structure use three unscaled ground motion records recently recorded in Italy and selected from the ITalian ACcelerometric Archive—ITACA [36]. The records are selected to be spectrum-compatible with the Uniform Hazard Spectrum (UHS) corresponding to a return period T_R of 475 years and a rigid soil (cat. A) site located at long 45.419, lat 7.1536. Additionally, according to EC8 [1] and NTC18 [31], for each period T_i included in a range between 0.02 s and 1.0 s, the average spectrum of the three selected records was greater than 90% of the UHS and lower than the 130% of the UHS, as indicated in Figure 8.

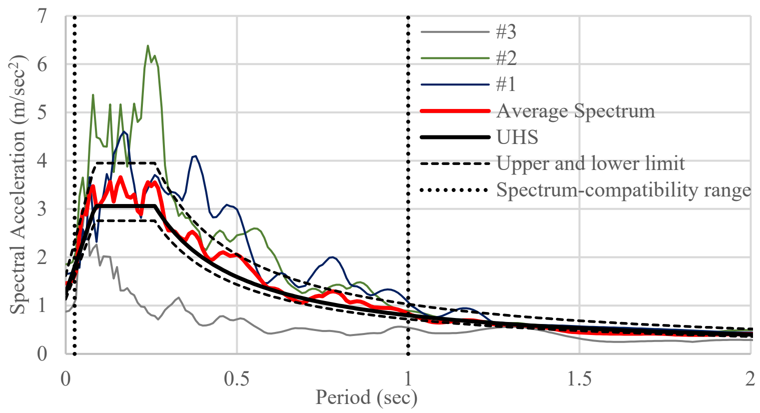

Figure 8. Response spectra corresponding to the horizontal components of the spectrum-compatible. Upper and lower limits represent 130% and 90% of the UHS considered in this study.

First, only the Horizontal component H of the ground motion is applied to the two-dimensional (2D) structure; then, the horizontal and vertical components (H + V) are applied simultaneously. For each ground motion component, 15 s of the record is used in the analysis to reduce the computational effort. This interval time is selected based on the significant duration of the record and considering the time over which a proportion of the total Arias Intensity between 5% and 95% is accumulated. Figure 9 shows the ground motion components H and V used for each record in this study.

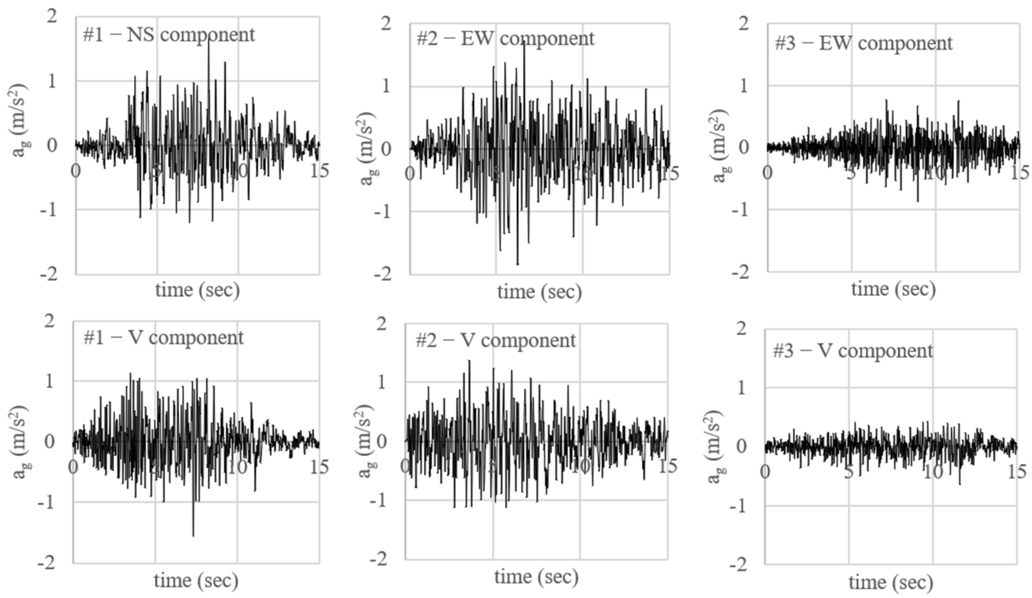

Figure 9. Horizontal (top row) and vertical (bottom row) recorded accelerograms: (**a**) earthquake #1, Norcia 30 October 2016, 14.9 km from the epicentre; (**b**) #2 Norcia 30 October 2016, 19.2 km from the epicentre; and (**c**) #3 Norcia 30 October 2016, 20 km from the epicentre.

Table 4 reports the main seismological features of each selected record (Name, Moment Magnitude M_w, Earthquake Date, Code of the Station, Site Class, and Epicentral Distance R) and the Peak Ground Acceleration of the selected horizontal component (PGA_H) and vertical components (PGAv).

Table 4. Ground motion records.

#	Event Name	Event M_w	Event Date	Station ID	EC8 Site Class	R (km)	PGA_H (g)	PGA_V (g)
1	Norcia	6.5	2016/10/30	CSC	B	14.900	0.169	0.159
2	Norcia	6.5	2016/10/30	MMO	A	19.200	0.189	0.140
3	Norcia	6.5	2016/10/30	T1215	A	20.100	0.089	0.065

The ratios PGA_V/PGA_H of the records #1, #2, and #3 are equal to 0.94, 0.74, and 0.73, respectively.

Figure 10 shows the response spectra of the H and V components of the three selected records and the corresponding ratio, V/H. These plots indicate that record #1 is characterized by a very high vertical spectral acceleration at T = 0.09 s, equal to $S_{a,V}$ = 5.20 m/s^2. For the same period, the horizontal spectral acceleration, $S_{a,H}$, is low; thus, the ratio at $S_{a,V}/S_{aH}$ is at its maximum in this period and is equal to 2.25. Analogous behaviour can be observed for records #2 and #3, whose maximum ratios $S_{a,V}/S_{aH}$ occur at T = 0.75 s and T = 0.59 s, respectively. As indicated in Section 3, the vertical period obtained for VL-c (T = 0.861 s) is very similar to the period corresponding to the maximum spectral amplification of record #1. This indicates that the effect of the vertical component of record #1 is, in this case, affected by an amplification due to the dynamic characteristics of the structure. This effect is negligible for the other records.

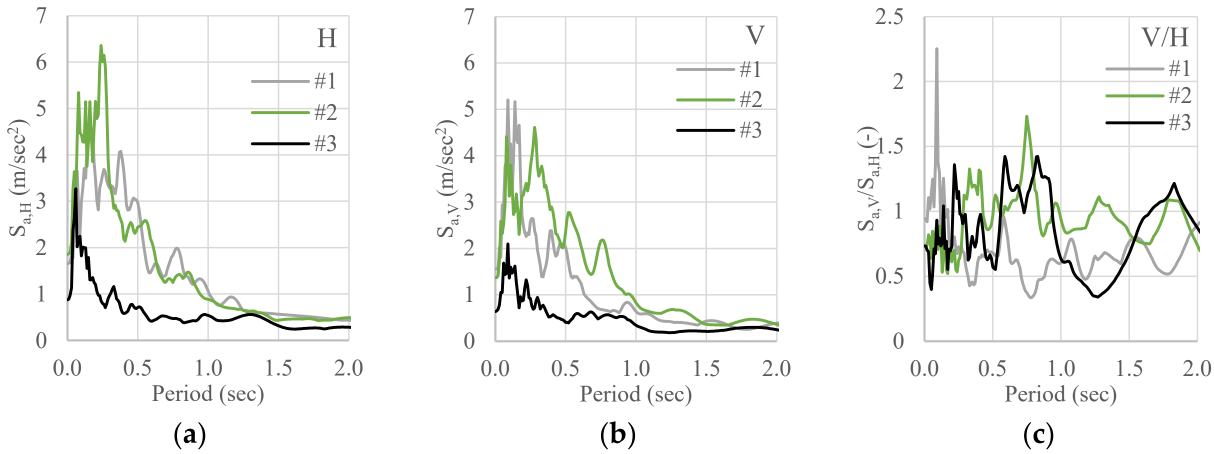

Figure 10. Response spectra of the H component (**a**) and V component (**b**) and ratio V/H for each period of the selected ground motion records (**c**).

5.2. Ground Motion Parameters of the Selected Records

The H and V components of the three selected earthquake ground motions are carefully analysed by six different intensity parameters, some of which are calculated from the ground motion records and others from the response spectra. The parameters computed from the ground motion records are PGA, Peak Ground Velocity (PGV), Arias Intensity (AI) [37], and Specific Energy Density (SED). PGA corresponds to the peak of the accelerogram, while PGV corresponds to the peak of the velocigram. AI is a cumulative ground motion Intensity Measure (IM), computed based on the time integral of the squared acceleration, as shown in Equation (5), where $a(t)$ is the ground motion acceleration at time t, $t_{\max}$ is the total duration of the ground motion, and g is the acceleration of gravity.

$$\mathrm{AI} = \frac{\pi}{2g}\int_0^{t_{\max}} [a(t)]^2 dt \tag{5}$$

Similarly, SED is computed on the time interval of the squared velocity, as shown in Equation (6), where $v(t)$ is the ground motion velocity.

$$\mathrm{SED} = \int_0^{t_{\max}} [v(t)]^2 dt \tag{6}$$

The parameters computed from the response spectra are the following: Acceleration spectrum Intensity (ASI) [38] and Housner Intensity (HI) [39]. ASI is defined as the integral of the pseudo-spectral acceleration (S_a) over the period range of 0.1–0.5 s, as given by Equation (7), where S_a is the 5% damped spectral acceleration at vibration period T.

$$\mathrm{ASI} = \int_{0.1}^{0.5} S_a(\xi = 0.05; \mathrm{T})dT \tag{7}$$

Similarly, HI is the integral of the pseudo-spectral velocity (S_v) over the period range of 0.1–0.5 s.

$$\mathrm{HI} = \int_{0.1}^{0.5} S_v(\xi = 0.05; \mathrm{T})dT \tag{8}$$

Table 5 shows the values of the above-described intensity parameters calculated for the H and V components of ground motions #1, #2, and #3.

Table 5. Ground motion parameters of the H and V components of #1, #2, and #3 ground motion records.

Ground Motion Parameters	#1		#2		#3	
	H	V	H	V	H	V
PGA (m/s^2)	0.872	0.640	1.653	1.558	1.853	1.369
PGV (m/s)	0.058	0.053	0.136	0.073	0.089	0.114
AI (m/s)	0.086	0.047	0.308	0.243	0.521	0.360
SED (m^2/s)	0.0026	0.0051	0.0253	0.0072	0.0189	0.0151
ASI (m/s)	0.404	0.335	1.400	1.014	1.499	1.254
HI (m)	0.166	0.137	0.378	0.251	0.350	0.314

In order to establish the record characterized by the maximum ground motion intensity for both seismic components, the Ground Motion Parameters (GMPs) of records #2 and #3 (GMP#i) are normalized to the corresponding GMPs of record #1 (GMP#1) (Figure 11). The ratio GMP#i/ GMP#1 shows that the GMPs of record #3 are consistently lower than those of the other two records for both seismic components. Conversely, the normalized GMPs of H components of records #1 and #2 can be greater than or less than one, depending on the GMP. In particular, the GMPs that involve acceleration terms (PGA, AI, and ASI) are greater than one, while GMPs with velocity terms (PGV, SED, and ASI) are lower than one.

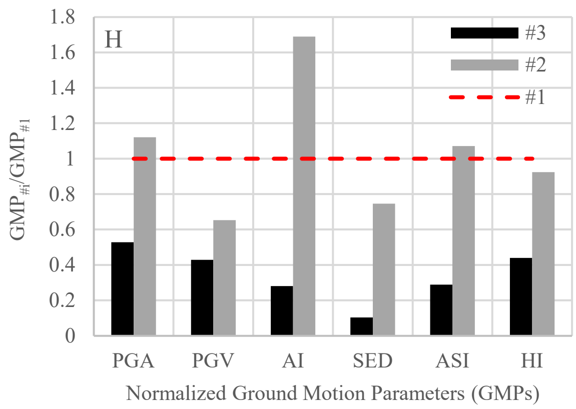

(**a**)

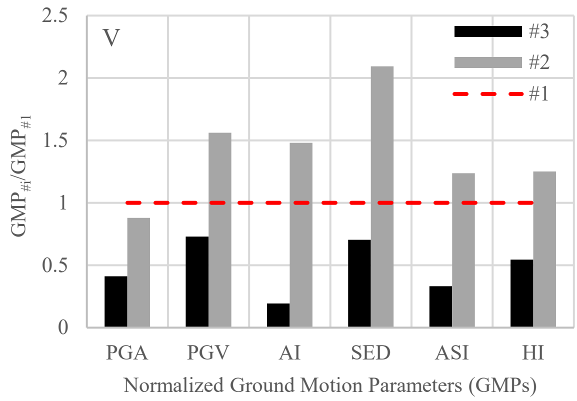

(**b**)

Figure 11. Normalized GMPs of the H component (**a**) and the V component (**b**) of the selected ground motion records.

The normalized GMPs of the V components of record #2 are almost always greater than one, except for PGA, for which the ratio GMP#2/GMP#1 equals 0.879. In short, this analysis shows that: (1) the H and V intensities of record #3 are always the lowest, (2) the V intensity of record #2 is almost always the highest (except for the PGA), and (3) there is not a record characterized by the highest H intensity, because it depends on the GMP.

5.3. Results Obtained for a Reference Masonry Pier

Figures 12–14 report the IDRs of masonry pier P1 (IDR_{P1}) obtained by varying the vertical load and subjecting the case–study structure to earthquakes #1, #2, and #3. Each figure reports the IDRs versus time curves of P1 for the VL-a (a), VL-b (b), and VL-c (c). The red lines indicate the 2% IDR limit (drift limit representative of the failure condition), while the black and grey lines represent the results with and without the vertical seismic component.

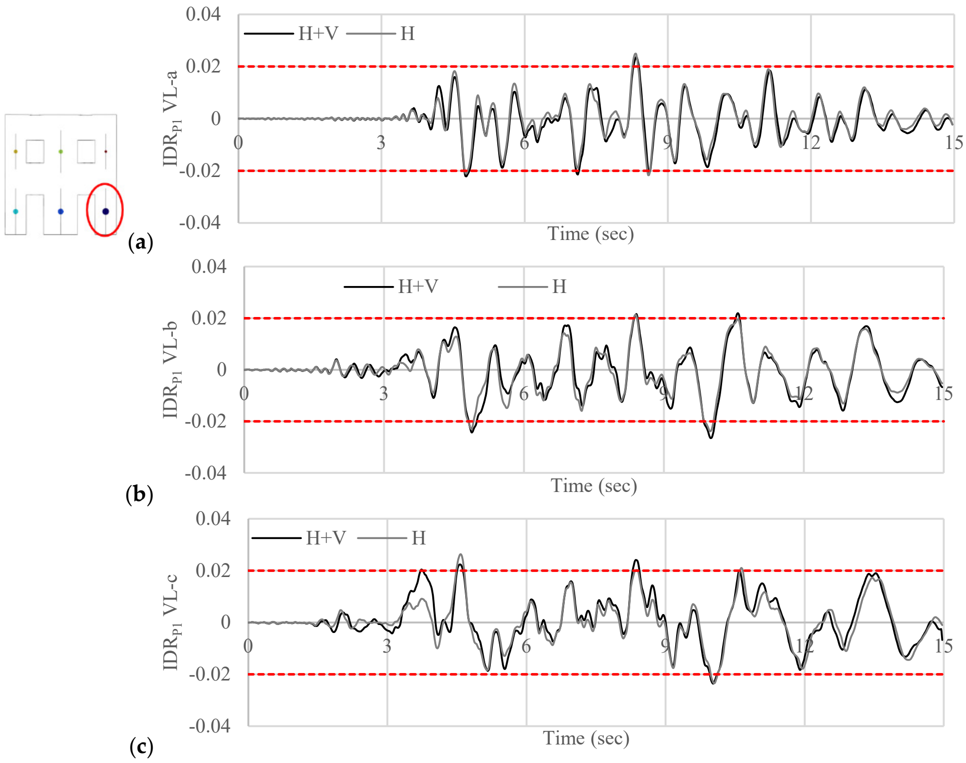

Figure 12. IDRs obtained subjecting the structure with VL-a (**a**), VL-b (**b**), and VL-c (**c**) to earthquake #1. The red lines indicate the IDR limit of 2%.

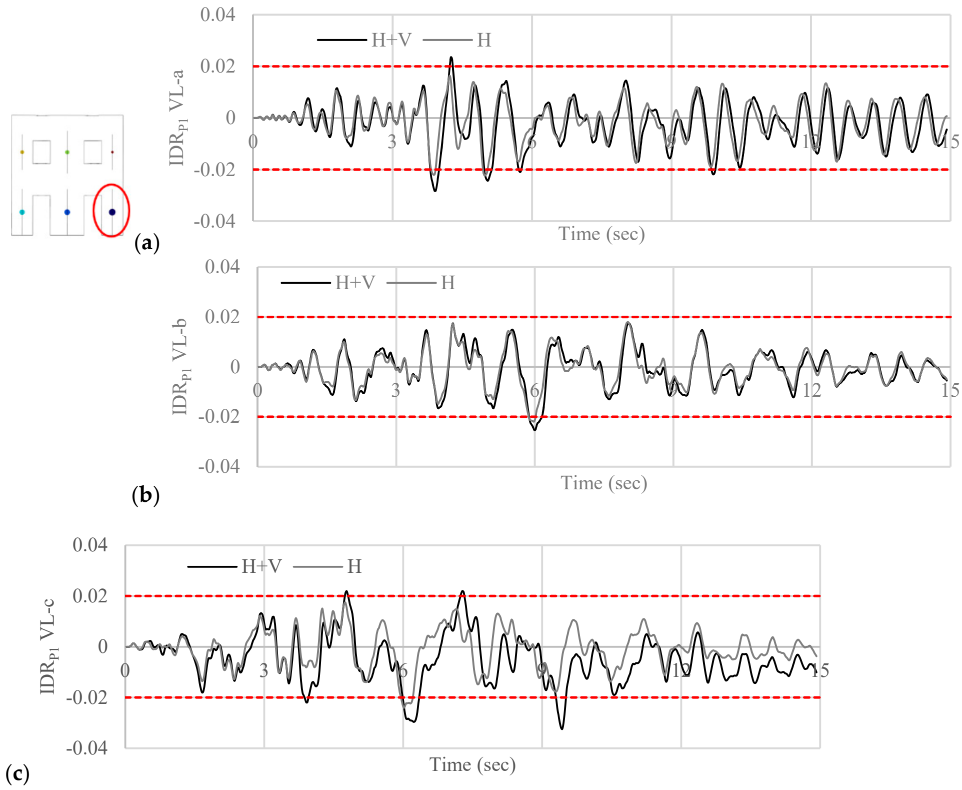

Figure 13. IDRs obtained subjecting the structure with VL-a (**a**), VL-b (**b**), and VL-c (**c**) to earthquake #2. The red lines indicate the IDR limit of 2%.

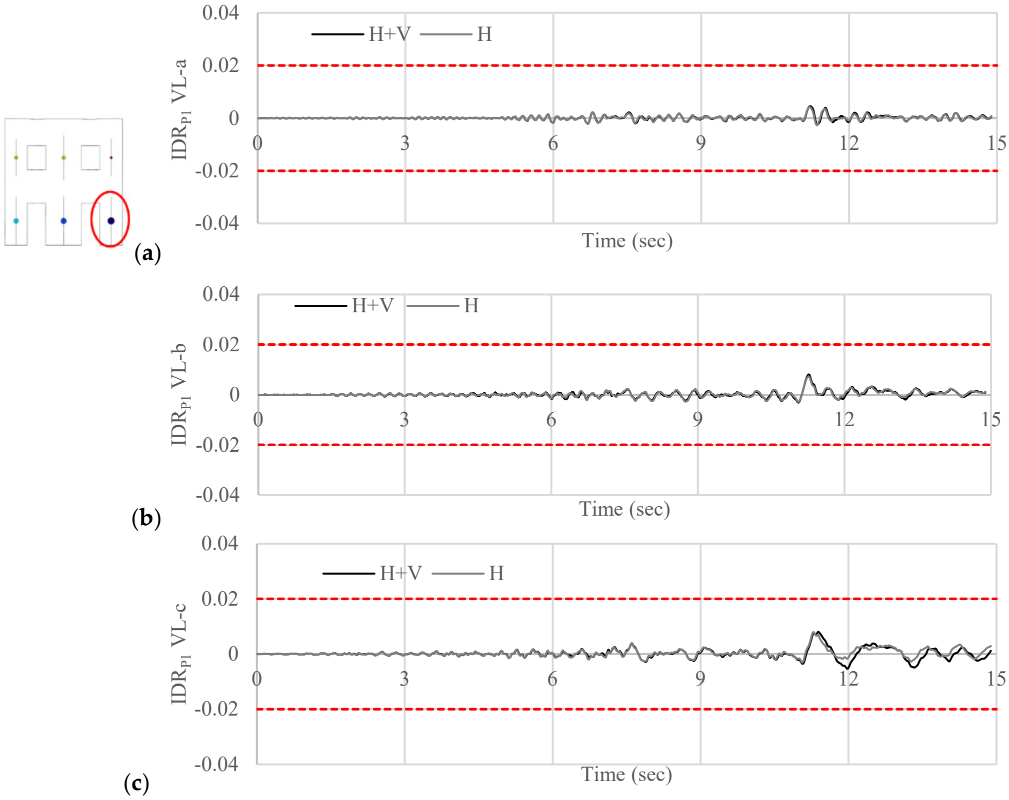

Figure 14. IDRs obtained subjecting the structure with VL-a (**a**), VL-b (**b**), and VL-c (**c**) to earthquake #3. The red lines indicate the IDR limit of 2%.

The figures show that the vertical component of the earthquakes tends to increase the IDR of the pier, especially for high vertical loads. The differences between results with or without the V component may depend on GMPs. This is shown, for example, by the comparison of IDR time histories in Figure 13c, with significant differences between the grey and black curves and IDR time histories in Figure 12c, with minor differences between the two curves, even though the two earthquakes have similar PGAs and the same loading condition.

Earthquake #3, characterized by a lower PGA than earthquakes #1 and #2, generates significantly lower IDRs (Figure 11), which never exceed the 1% value.

Figures 15–17 show the IDR-V_b curve obtained on masonry pier P1 and the damage pattern when the structure is subjected to earthquakes #1, #2, and #3. Each figure reports these results with and without the V component and for the different loading conditions (VL-a (a), VL-b (b) 10%, and VL-c (c)).

The obtained results confirm that the V component of the earthquakes increases the EDPs, and this increase becomes more significant as the vertical load and the value of the IDR increase. As with the shear–displacement curves, the damage scenario indicates more extensive damage when the vertical seismic component is considered, particularly for high vertical loads.

Note that, although earthquake #3 generates a limited damage scenario (Figure 17) compared to those obtained from earthquakes #1 (Figure 15) and #2 (Figure 16), there is still a widespread crack pattern when the V component of the earthquake is taken into account.

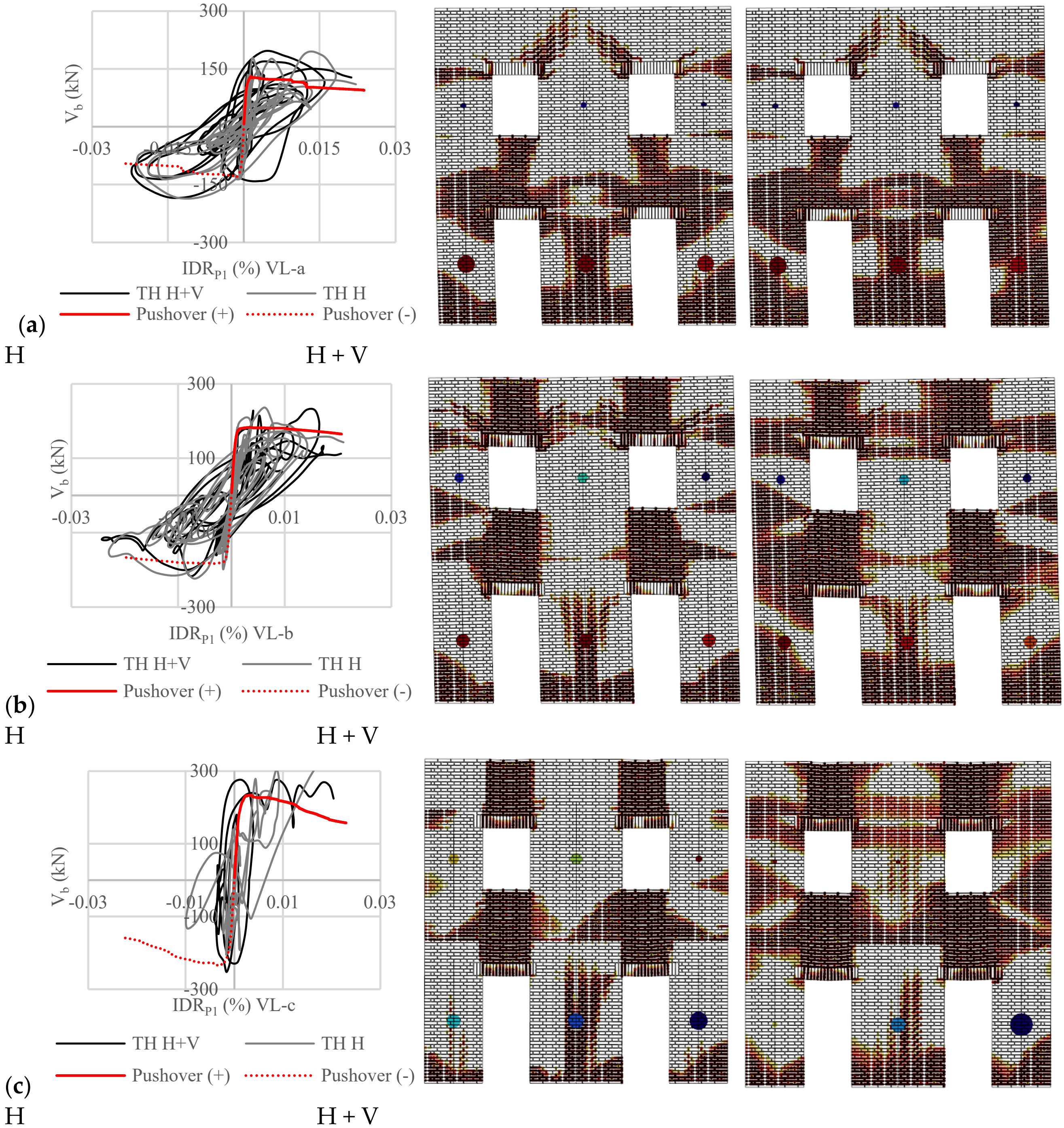

Figure 15. IDR-V_b curves and crack patterns obtained for earthquake #1. TH results for the H component are in grey, TH results for H + V components are in black, the PO curve for positive displacements is the continuous red line, and the PO curve for negative displacements is the dashed red line. Loading conditions: VL-a (**a**), VL-b (**b**), and VL-c (**c**).

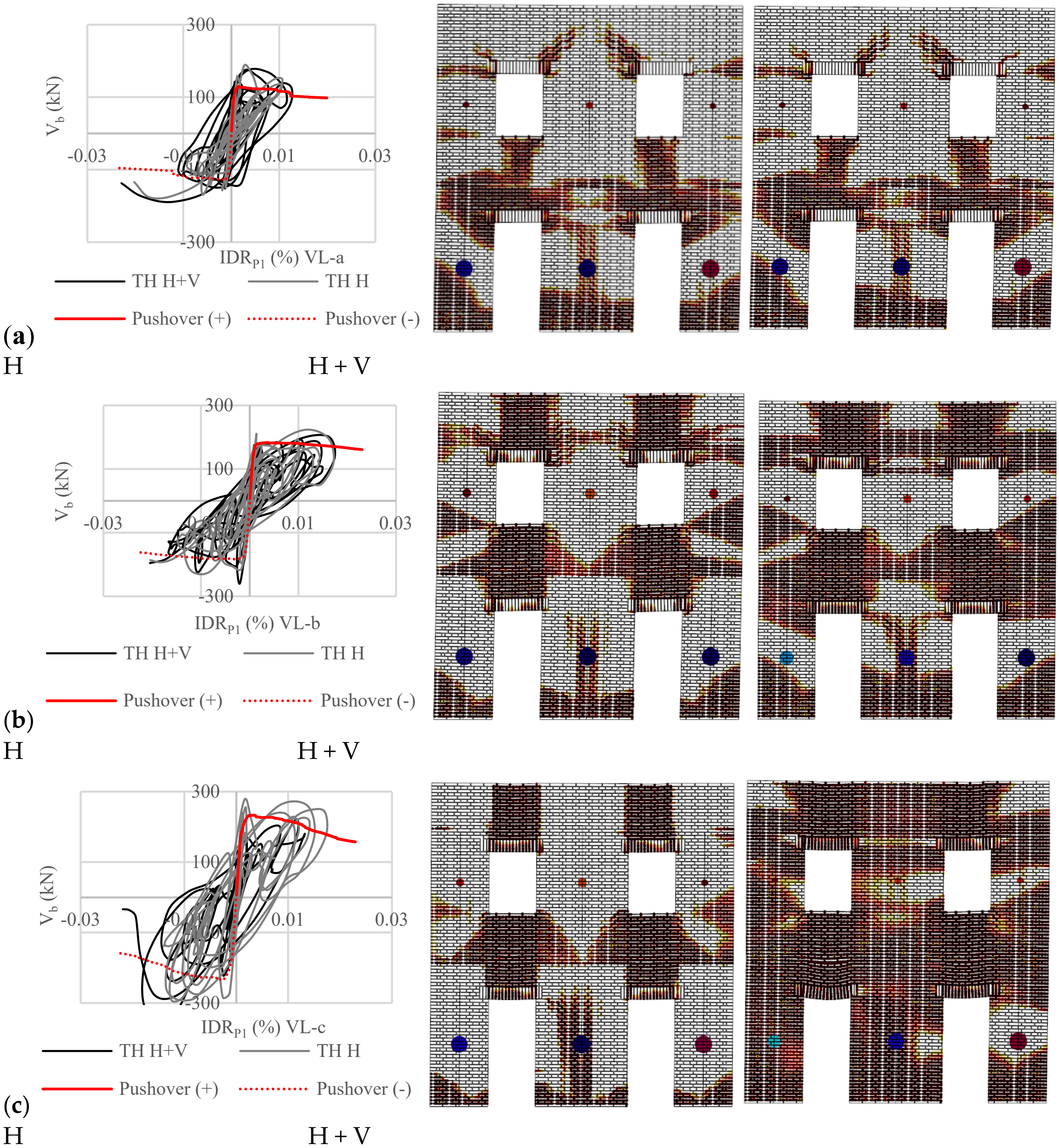

Figure 16. IDR-V_b curves and crack patterns obtained for earthquake #2. TH results for the H component are in grey, TH results for H + V components are in black, the PO curve for positive displacements is the continuous red line, and the PO curve for negative displacements is the dashed red line. Loading conditions: VL-a (**a**), VL-b (**b**), and VL-c (**c**).

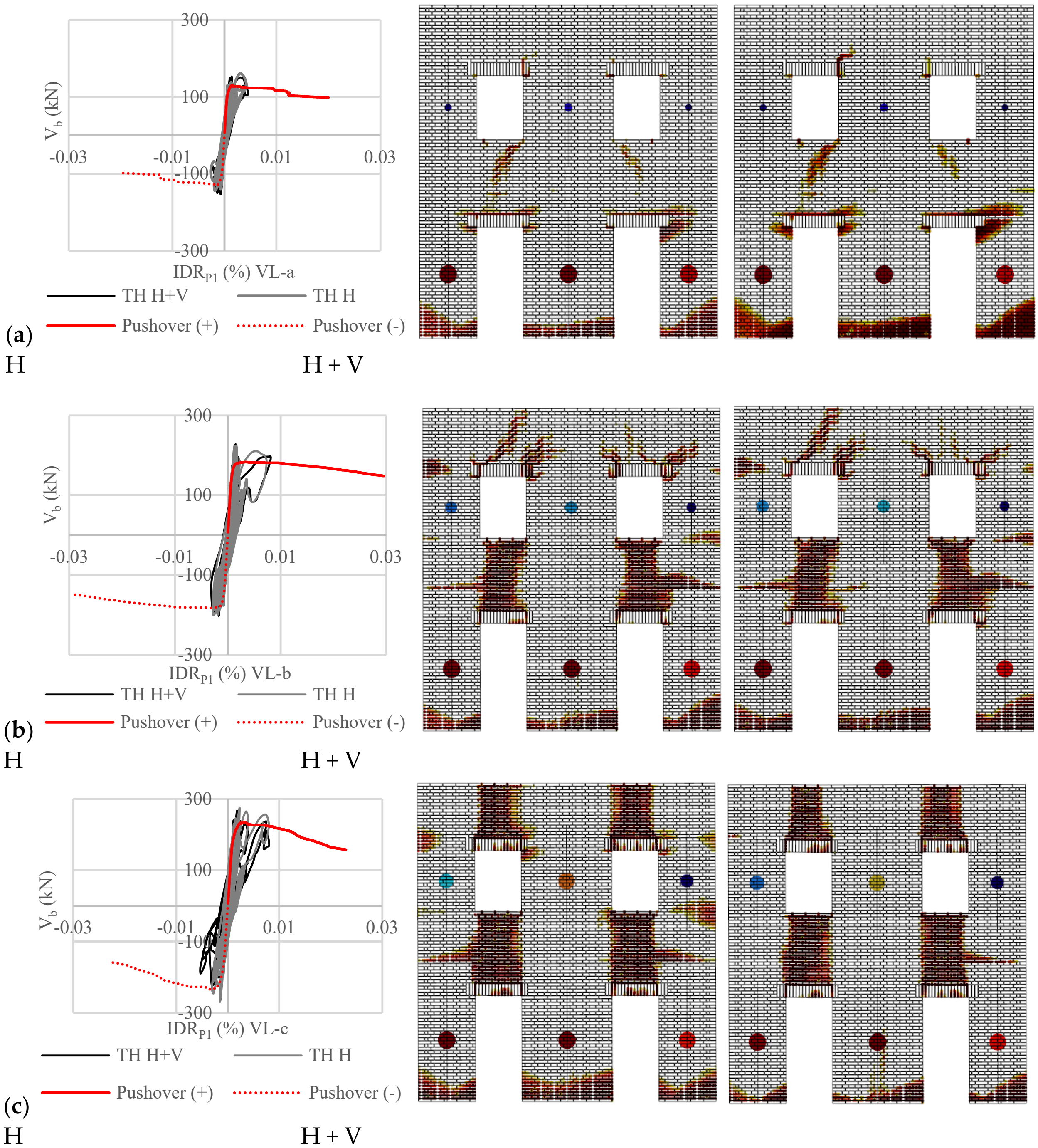

Figure 17. IDR-V_b curves and crack patterns obtained for the earthquake #1. TH results for the H component are in grey, TH results for H + V components are in black, the PO curve for positive displacements is the continuous red line, and the PO curve for negative displacements is the dashed red line. Loading conditions: VL-a (**a**), VL-b (**b**), and VL-c (**c**).

5.4. Correlation between the Ground Motion Parameters and Engineering Demand Parameters

To evaluate the possible correlations between the GMPs of the V components (GMP_V) and the Inter-story Drift Ratios (IDRs) obtained for the case–study structure, the maximum IDRs obtained from the simultaneous application of the H and V components, maxIDR(H + V), are related with the GMP_V shown in Table 5 [40]. Figure 18 shows six plots, where the values of PGA_V, PGV_V, AI_V, SED_V, ASI_V, and HI_V of records #1, #2, and #3 are displayed on the horizontal axis, and on the vertical axis, the values of the maxIDR(H + V) obtained applying VL-a (in black), VL-b (in orange), and VL-c (in grey) on masonry pier P1 are shown. Similarly, Figures 19–21 show the same plots for IDR_{S1}, IDR_{S2}, and the RDR.

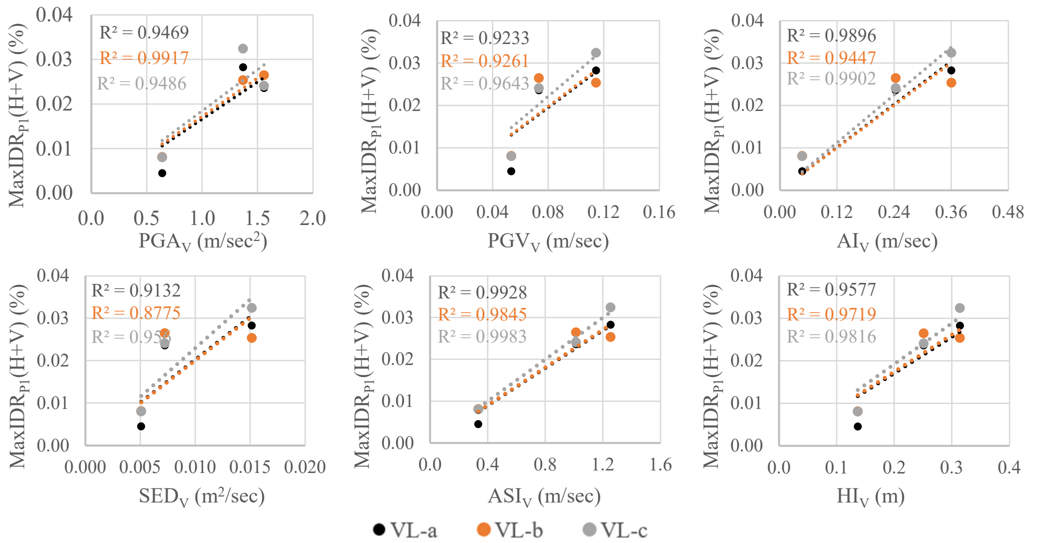

Figure 18. Correlations between the GMPs of the V components (GMP_V) and the maximum IDR obtained on masonry pier P1 from the simultaneous application of the H and V components, $maxIDR_{P1}$(H + V). In each image, with the sole exception of the PGA_V plot, from left to right, earthquakes #3, #1, and #2; in the PGA_V plot (**top left**), from left to right, earthquakes #3, #2, and #1.

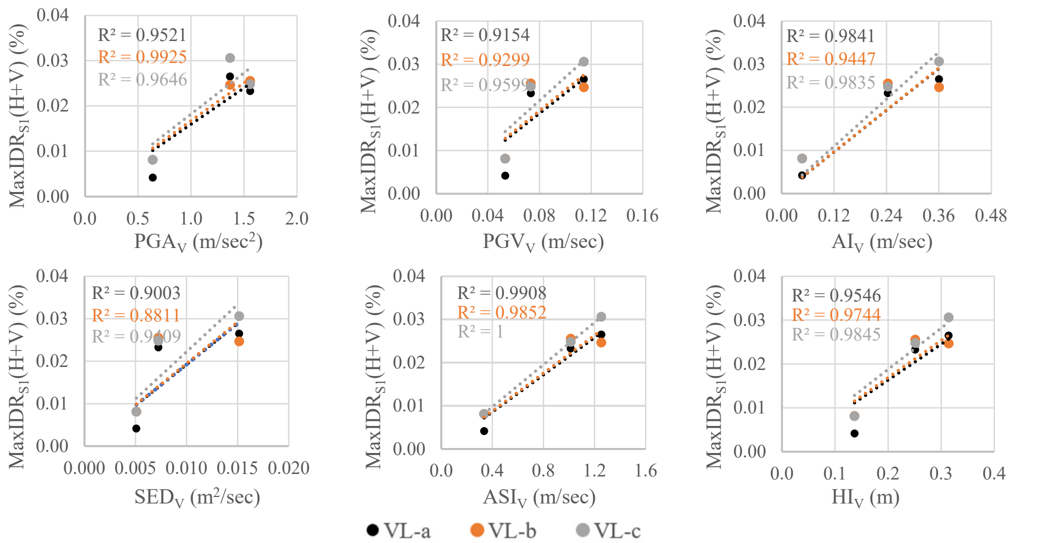

Figure 19. Correlations between the GMPs of the V components (GMP_V) and the maximum IDR obtained on the first story of the case–study structure from the simultaneous application of the H and V components, $maxIDR_{S1}$(H + V). In each image, with the only exception of PGA_V plot, from left to right, earthquakes #3, #1, and #2; in the PGA_V plot (**top left**), from left to right, earthquakes #3, #2, and #1.

The correlations between GMP_V and maxIDRs are calculated using the Coefficient of Determination R^2, a number between 0 and 1 that measures how well a statistical model predicts an outcome. The values of coefficients R^2 are based on linear regression lines fitted through the data, characterized by the form $y = ax$, where a is a constant coefficient.

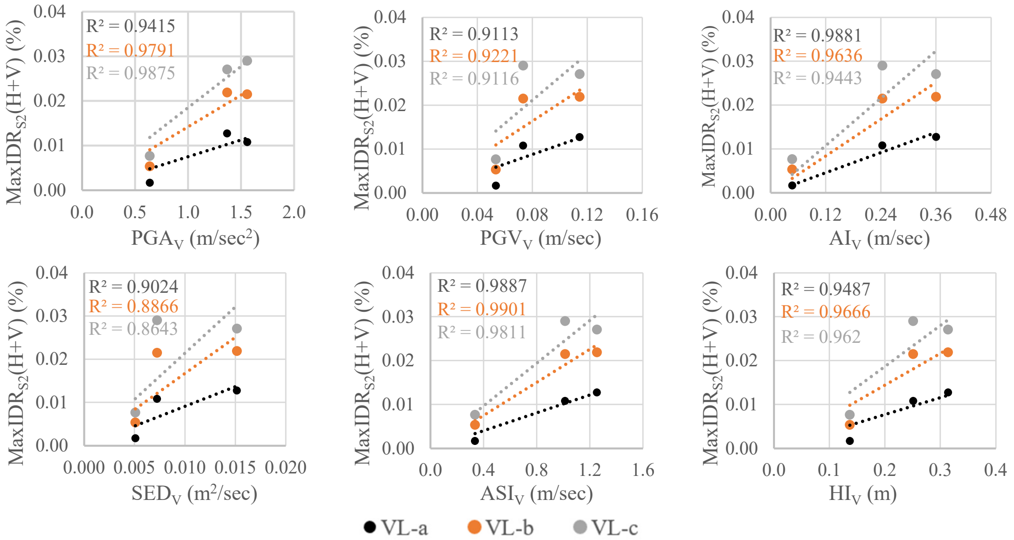

Figure 20. Correlations between the GMPs of the V components (GMP_V) and the maximum IDRs obtained for the second story of the case–study structure from the simultaneous application of the H and V components, $maxIDR_{S2}(H + V)$. In each image, with the only exception of the PGA_V plot, from left to right, earthquakes #3, #1, and #2; in the PGA_V plot (**top left**), from left to right, earthquakes #3, #2, and #1.

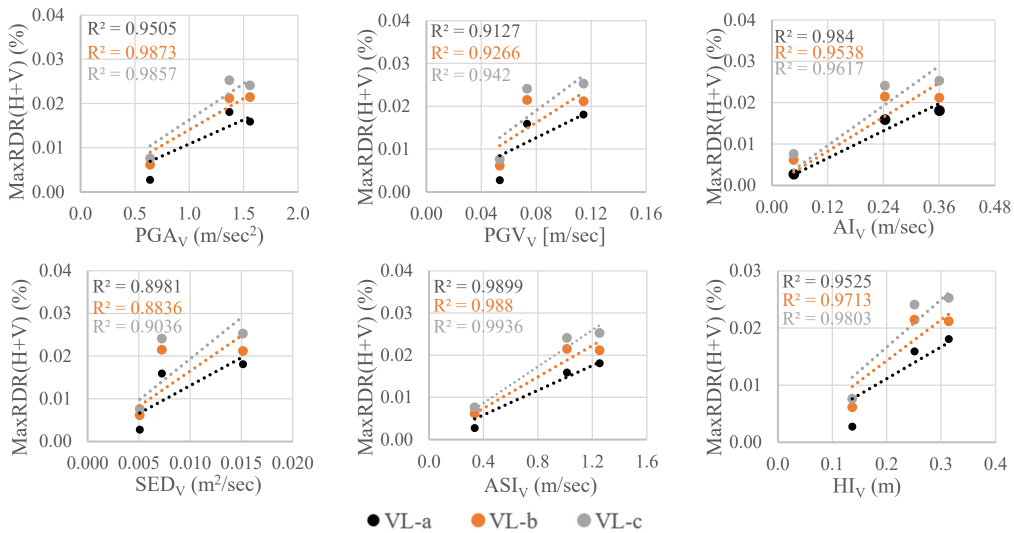

Figure 21. Correlations between the GMPs of the V components (GMP_V) and the maximum RDR obtained on the case–study structure from the simultaneous application of the H and V components, $maxRDR(H + V)$. In each image, with the sole exception of the PGA_V plot, from left to right, earthquakes #3, #1, and #2; in the PGA_V plot (**top left**), from left to right, earthquakes #3, #2, and #1.

The results obtained from this analysis show a very clear correlation between GMP_V and maxEDPs. All regression lines are characterized by a positive slope, demonstrating how, as the GMP_V increases, the corresponding structural demand increases. This indicates that the influence of the vertical component should be predicted by accurately selecting ground motion records with a significative intensity of the vertical ground motion component. Moreover, it is expected that, if a masonry structure is subjected to a sequence of earthquakes, the greater the intensity of the vertical component, the greater the structural demand.

Table 6 reports the numerical results obtained from the NTHAs for each considered record (#1, #2, and #3) and the vertical load case (VL-a, VL-b, and VL-c). The table includes the maxEDPs obtained considering only the H component and the simultaneous application of the H and V components. Moreover, for each case, it indicates the ratio (H + V)/H, corresponding to the percentage of increase/decrease of the maxEDPs due to the V component. Note that, unlike the graphic results shown in Figures 12–14, the increase of the ratio (H + V)/H with the vertical load is not observed. However, this result depends on how this ratio is calculated. In fact, the ratio (H + V)/H is calculated as the ratio between the maxEDP corresponding to the application of the H + V components and the maxEDP corresponding to the H component, whose values generally do not correspond to the same at the same time step t_i. For this reason, a further EDP is considered to account for the increment of the EDP time series due to the V component varying the vertical load.

Table 6. EDPs obtained applied to the case–study structure of the selected records with and without the vertical component.

EDPs	Load Case	Record #1			Record #2			Record #3		
		H	H+V	(H+V)/H	H	H+V	(H+V)/H	H	H+V	(H+V)/H
IDR_{P1}	VL-a	0.02484	0.02361	0.950	0.02229	0.02827	1.268	0.00419	0.00451	1.077
	VL-b	0.02382	0.02647	1.111	0.02195	0.02536	1.155	0.00733	0.00812	1.108
	VL-c	0.02635	0.02409	0.914	0.02404	0.03242	1.349	0.00797	0.00804	1.009
IDR_{S1}	VL-a	0.02450	0.02329	0.951	0.02090	0.02652	1.269	0.00390	0.00419	1.072
	VL-b	0.02354	0.02554	1.085	0.02182	0.02466	1.130	0.00739	0.00813	1.100
	VL-c	0.02664	0.02480	0.931	0.02388	0.03060	1.282	0.00807	0.00813	1.007
IDR_{S2}	VL-a	0.01018	0.01082	1.063	0.01017	0.01276	1.254	0.00178	0.00170	0.956
	VL-b	0.01989	0.02149	1.081	0.01950	0.02190	1.123	0.00535	0.00536	1.002
	VL-c	0.02340	0.02900	1.239	0.02073	0.02708	1.306	0.00706	0.00767	1.086
RDR	VL-a	0.01621	0.01590	0.981	0.01491	0.01807	1.212	0.00262	0.00273	1.043
	VL-b	0.01990	0.02147	1.079	0.01909	0.02119	1.110	0.00578	0.00614	1.063
	VL-c	0.02398	0.02410	1.005	0.02137	0.02527	1.183	0.00736	0.00762	1.034

For each step t_i of the ground motion time histories, the geometrical distance between the EDP with and without vertical component is calculated, and subsequently, the maximum values over the entire time history are obtained as indicated in Equation (9).

$$\max\delta = \max\sqrt{[EDP_{H+V}(t_i) - EDP_H(t_i)]^2} \tag{9}$$

Figure 22 and Table 7 show the values of maxδ varying the vertical load for IDR_{S1} (a), IDR_{S2} (b), and the RDR (c).

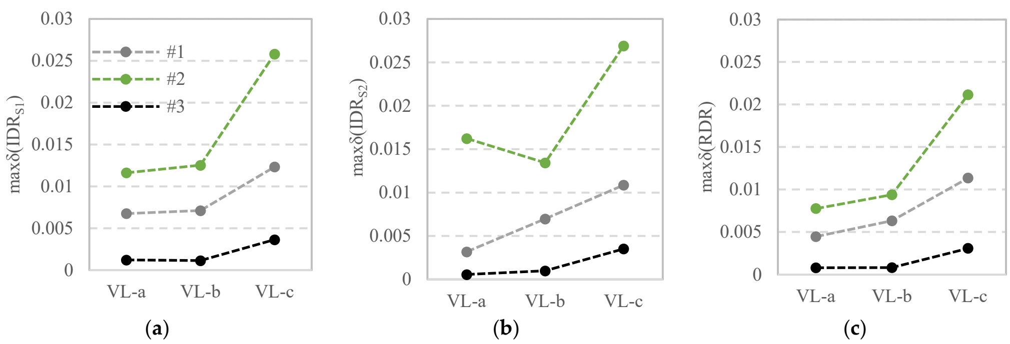

Figure 22. Maximum distance δ between the EDPs obtained with and without the vertical component for VL-a, VL-b, and VL-c. On the left (**a**), the maxδ obtained from $IDRs_1$, in the centre (**b**), the maxδ obtained from $IDRs_2$ and on the right (**c**), the maxδ obtained from the RDR.

Table 7. Maximum values of the geometrical distance between the EDPs calculated over each time history with and without the vertical component.

maxδ	**Record #1**			**Record #2**			**Record #3**		
	VL-a	**VL-b**	**VL-c**	**VL-a**	**VL-b**	**VL-c**	**VL-a**	**VL-b**	**VL-c**
Maxδ (IDR_{S1})	0.00676	0.00710	0.01234	0.01163	0.01254	0.02582	0.00121	0.00114	0.00364
Maxδ (IDR_{S2})	0.00319	0.00698	0.01087	0.01623	0.01344	0.02690	0.00057	0.00099	0.00352
Maxδ (RDR)	0.00447	0.00632	0.01136	0.00777	0.00939	0.02115	0.00080	0.00081	0.00308

The figure shows that, for all EDPs and almost all ground motion records (#1, #2, and #3), the maxδ value increases as the vertical load on the structure increases. This indicates that the effect of the vertical component is strongly affected by the vertical load acting on the structure. The only exception to this behaviour is for the maxδ obtained from IDR_{S2} with earthquake #2. In this case, the maxδ decreases for VL-b with respect to VL-a and VL-c. However, this does not invalidate the general results on the influence of the vertical component, as the load increases as a significative increase of maxδ is still observed between VL-a and VL-c.

Figure 22 also shows that earthquakes #2, #1, and #3 provide the largest, middle, and lowest EDP values, in that order. These results confirm that, regardless of the applied load, the influence of the vertical component increases with its intensity. Section 5.2 showed that, with only the exception of the PGA, for all other GMPs, the vertical components of earthquakes #2 and #3 are characterized by the maximum and minimum intensities, respectively (Figure 11).

6. Conclusions

This paper investigates the effect of the vertical seismic component on the capacity and damage scenario of unreinforced masonry structures. Pushover and nonlinear time history analyses are carried out for a two-story regular wall described with a detailed micro-modelling approach under different dead loads representative of typical stress states.

Nonlinear time history analyses (NTHAs) were carried out using three unscaled ground motion records recently recorded in Italy and selected from the ITalian ACcelerometric Archive—ITACA [36]. The records were selected to be spectrum-compatible with the Uniform Hazard Spectrum (UHS) corresponding to a return period TR of 475 years and a rigid soil (cat. A). The recorded ground motions were applied to the case–study structure with and without the vertical component (V) of the seismic acceleration.

Two global Engineering Demand Parameters (EDPs) were considered for the NTHA: the Inter-story Drift Ratio (IDR) and the Roof Drift Ratio (RDR), which represent the ratio between the inter-story displacement and the story height and the ratio between the displacement on the top of the structure and its total height. In addition, the behaviour of the single masonry pier varying the vertical load and the IDR of the masonry pier P1 is considered as further EDP.

The correlation between the Engineering Demand Parameters (inter-story drift and roof drift ratios) and the Ground Motion Parameters (GMPs) of the horizontal and vertical components was discussed. The influence of the vertical component was highlighted by the apparent correlation between the GMPs of the vertical component and the calculated EDPs.

For each step t_i of the ground motion time histories, the geometrical distance between a given EDP with and without the vertical component was also calculated, and its maximum values (max δ) over the entire time history were introduced as a new parameter that was found to be very closely correlated to the GMPs and to the vertical load.

This indicates that the vertical ground motion component cannot be a priori neglected for URM walls when moderate-to-large vertical GMPs are expected, as confirmed by a comparison of damage scenarios obtained with and without the vertical component of the earthquake.

Future developments of this work include using additional accelerograms and analysing the role of vertical components of earthquakes for irregular masonry walls and 3D structures, as well as for masonry structures modelled with the equivalent frame approach [41–44].

Author Contributions: Conceptualisation, G.C., A.D.P. and V.S.; methodology, G.C., A.D.P., V.S. and C.C.; software, G.C., A.D.P. and C.C.; validation, G.C., A.D.P., V.S. and C.C.; writing—original draft preparation, G.C., A.D.P., V.S. and C.C.; writing—review and editing, G.C., A.D.P., V.S. and C.C.; visualisation, A.D.P. and C.C.; and supervision, G.C. and V.S. All authors have read and agreed to the published version of the manuscript.

Funding: This research received no external funding.

Data Availability Statement: All relevant data are contained within the article.

Acknowledgments: The study presented in this article was partly developed within the activities of WP10 of the ReLUIS-DPC 2019–2021 research program of the Italian Civil Protection Agency (DPC). The opinions and conclusions presented by the authors do not necessarily reflect those of DPC and Reluis Consortium.

Conflicts of Interest: The authors declare no conflict of interest.

References

1. *Eurocode 8 EN 1998-1*; Design of Structures for Earthquake Resistance—Part 1: General Rules, Seismic Actions and Rules for Buildings. European Committee for Standardization: Brussels, Belgium, 2005.
2. *Eurocode 8 EN 1998-3*; Design of Structures for Earthquake Resistance—Part 3: Assessment and Retrofitting of Buildings. European Committee for Standardization: Brussels, Belgium, 2005.
3. Borgozia, Y.; Campbell, K.W. Characteristics of Free-Field Vertical Ground Motion during the Northridge Earthquake. *Earthq. Spectra* **1995**, *11*, 515–525. [CrossRef]
4. Borgozia, Y.; Niazi, M.; Campbell, K.W. Relationship between vertical and horizontal response spectra for the Northridge earthquake. In Proceedings of the Memorias, XI World Conference on Earthquake Engineering, Acapulco, Mexico, June 1996.
5. Borgozia, Y. Vertical response of twelve structures recorded during the Northridge earthquake. *Earthq. Spectra* **1998**, *14*, 411–432. [CrossRef]
6. Elgamal, A.; He, L. Vertical earthquake ground motion records: An overview. *J. Earthq. Eng.* **2004**, *8*, 663–697. [CrossRef]
7. Liberatore, D.; Doglioni, C.; Al Shawa, O.; Atzori, S.; Sorrentino, L. Effects of coseismic ground vertical motion on masonry constructions damage during the 2016 Amatrice-Norcia (Central Italy) earthquakes. *Soil Dyn. Earthq. Eng.* **2019**, *120*, 423–435. [CrossRef]
8. Sorrentino, L.; Liberatore, L.; Decanini, L.D.; Liberatore, D. The performance of churches in the 2012 Emilia earthquakes. *Bull. Earthq. Eng.* **2014**, *12*, 2299–2331. [CrossRef]
9. Carydis, P.; Castiglioni, C.; Lekkas, E.; Kostaki, I.; Lebesis, N.; Drei, A. The Emilia Romagna, May 2012 earthquake sequence. The influence of the vertical earthquake component and related geoscientific and engineering aspects. *Ing. Sismica* **2012**, *29*, 31–58.
10. De Nardis, R.; Filippi, L.; Costa, G.; Suhadolc, P.; Nicoletti, M.; Lavecchia, G. Strong motion recorded during the Emilia 2012 thrust earthquakes (Northern Italy): A comprehensive analysis. *Bull. Earthq. Eng.* **2014**, *12*, 2117–2145. [CrossRef]
11. Acito, M.; Bocciarelli, M.; Chesi, C.; Milani, G. Collapse of the clock tower in Finale Emilia after the May 2012 Emilia Romagna earthquake sequence: Numerical insight. *Eng. Struct.* **2014**, *72*, 70–91. [CrossRef]
12. Dana, M.; Cussen, A.; Chen, Y.N.; Davis, C.; Greer, M.; Houston, J.; Littler, P.; Roufegarinejad, A. Effects of the seismic vertical component on structural behavior—An analytical study of current code practices and potential areas of improvement. In Proceedings of the 10th National Conference in Earthquake Engineering, Earthquake Engineering Research Institute, Anchorage, AK, USA, 21–25 July 2014.
13. Bradley, B.A.; Quigley, M.C.; Van Dissen, R.J.; Litchfield, N.J. Ground Motion and Seismic Source Aspects of the Canterbury Earthquake Sequence. *Earthq. Spectra* **2014**, *30*, 1–15. [CrossRef]
14. Ghaffarzadeh, H.; Nazeri, A. The effect of the vertical excitation on horizontal response of structures. *Earthq. Struct.* **2015**, *9*, 625–637. [CrossRef]
15. Papazoglou, A.J.; Elnashai, A.S. Analytical and field evidence of the damaging effect of vertical earthquake ground motion. *Earthq. Eng. Struct. Dyn.* **1996**, *25*, 1109–1137. [CrossRef]
16. Di Michele, F.; Cantagallo, C.; Spacone, E. Effects of the vertical seismic component on seismic performance of an unreinforced masonry structures. *Bull. Earthq. Eng.* **2020**, *18*, 1635–1656. [CrossRef]
17. Chieffo, N.; Mosoarca, M.; Formisano, A.; Lourenco, P.B.; Milani, G. The effect of ground motion vertical component on the seismic response of historical masonry buildings: The case study of the Banloc Castle in Romania. *Eng. Struct.* **2021**, *249*, 113346. [CrossRef]
18. Rinaldin, G.; Fasan, M.; Noé, S.; Amadio, C. The influence of earthquake vertical component on the seismic response of masonry structures. *Eng. Struct.* **2019**, *185*, 184–193. [CrossRef]
19. Kallioras, S.; Graziotti, F.; Penna, A.; Magenes, G. Effects of the vertical ground motion on the dynamic response of URM structures: Comparative shake-table test. *Earthq. Eng. Struct. Dyn.* **2021**, *51*, 347–368. [CrossRef]

20. Chieffo, N.; Mosoarca, M.; Formisano, A.; Lourenco, P.B.; Milani, G. Seismic vulnerability assessment of a Romanian historical building under near-source earthquake. In Proceedings of the 12th International Conference on Structural Analysis of Historical Constructions SAHC, Barcelona, Spain, 16 September 2020.
21. Brunelli, A.; de Silva, F.; Piro, A.; Parisi, F.; Sica, S.; Silvestri, F.; Cattari, S. Numerical simulation on the seismic response and soil-structure interaction for a monitored masonry school building damage by the 2016 Central Italy earthquake. *Bull. Earthq. Eng.* **2021**, *19*, 1181–1211. [CrossRef]
22. Petracca, M.; Candeloro, F.; Camata, G. *STKO User Manual*; ASDEA Software Technology: Pescara, Italy, 2017.
23. Palatsu, B.; Gonen, S.; Parisi, F.; Erdogmus, E.; Tuncay, K.; Funari, M.C.; Lourenco, P.B. Probabilistic approach to assess URM walls with openings using discrete rigid block analysis (D-RBA). *J. Build. Eng.* **2022**, *61*, 105269. [CrossRef]
24. Gonen, S.; Pulatsu, B.; Erdogmus, E.; Lourenco, P.B. Effects of spatial variability and correlation in stochastic discontinuum analysis of unreinforced masonry walls. *Constr. Build. Mater.* **2022**, *337*, 127511. [CrossRef]
25. Petracca, M.; Pelà, L.; Rossi, R.; Zaghi, S.; Camata, G.; Spacone, E. Micro-scale continuous and discrete numerical models for nonlinear analysis of masonry shear walls. *Constr. Build. Mater.* **2017**, *149*, 296–314. [CrossRef]
26. Petracca, M.; Camata, G.; Spacone, E.; Pelà, L. Efficient Constitutive model for continuous micro-modeling of masonry structures. *Int. J. Arch. Heritage* **2022**, *17*, 134–146. [CrossRef]
27. McKenna, F. OpenSees: A framework for earthquake engineering simulation. *Comput. Sci. Eng.* **2011**, *13*, 58–66. [CrossRef]
28. Magenes, G.; Kingsley, G.; Calvi, G.M. Seismic Testing of a Full-Scale, Two-Story Masonry Building: Test Procedure and Measured Experimental Response. *Techol. Rep.* **1995**. [CrossRef]
29. Magenes, G. Shear-compression testing and analysis of brick masonry walls. In *Proceedings of the 10th European Conference on Earthquake Engineering*; Central Institute for Meteorology and Geodynamics: Vienna, Austria, 1995; Volume 3, pp. 1657–1662.
30. Canizzaro, F.; Castellazzi, G.; Grillada, N.; Pantò, B.; Petracca, M. Modelling the nonlinear static response of a 2-storey URM benchmark case study: Comparison among different modelling strategies using two- and three-dimensional elements. *Bull. Earthq. Eng.* **2022**, *20*, 2085–2114. [CrossRef]
31. *G.U. n.42 of 20/2/2018*; Italian Technical Code, Decreto Ministeriale 17/1/2018. Aggiornamento delle Norme Tecniche per le Costruzioni. Ministry of Infrastructures and Transportation: Rome, Italy, 2018. (In Italian)
32. Circolare n. 7 del 21 Gennaio 2019 (2019) Istruzioni per l'applicazione dell' ≪Aggiornamento delle "Norme tecniche per le costruzioni"≫ di cui al DM 17 gennaio 2018.
33. Turnšek, F.; Čačovič, F. Some experimental results on the strength of brick masonry walls. In Proceedings of the 2nd International Brick Masonry Conference, Stoke-on-Trent, UK, 12–15 April 1970.
34. *CNR DT 212/2013*; Istruzioni per la Valutazione Affidabilistica della Sicurezza Sismica di Edifici Esistenti. Consiglio Nazionale Delle Ricerche: Roma, Italy, 2014.
35. Cantagallo, C.; Camata, G.; Spacone, E. A Probability-based Approach for the Definition of the Expected Seismic Damage Evaluated with Non-linear Time-History Analyses. *J. Earthq. Eng.* **2019**, *23*, 261–283. [CrossRef]
36. Russo, E.; Felicetta, C.D.; Amico, M.; Sgobba, S.; Lanzano, G.; Mascandola, C.; Pacor, F.; Luzi, L. *Italian Accelerometric Archive v3.2*; Dipartimento della Protezione Civile Nazionale, Istituto Nazionale di Geofisica e Vulcanologia: Bologna, Italy, 2022. [CrossRef]
37. Arias, A. Arias, A. A measure of earthquake intensity. In *Seismic Design for Nuclear Power Plants*; Hansen, R.J., Ed.; MIT Press: Cambridge, MA, USA, 1970; pp. 438–483.
38. Von Thun, J.L.; Rochim, L.H.; Scott, G.A.; Wilson, J.A. Earthquake ground motions for design and analysis of dams. *Earthq. Eng. Soil Dyn. II* **1988**, *8*, 463–481.
39. Housner, G.W. Intensity of ground motion during strong earthquakes. In *Second Technical Report*; California Institute of Technology: Pasedena, CA, USA, 1952.
40. Cantagallo, C.; Camata, G.; Spacone, E.; Corotis, R. The variability of deformation demand with ground motion intensity. *Probabilistic Eng. Mech.* **2012**, *28*, 59–65. [CrossRef]
41. Siano, R.; Sepe, V.; Camata, G.; Spacone, E.; Roca, P.; Pelà, L. Analysis of the performance in the linear field of Equivalent-Frame Models for regular and irregular masonry walls. *Eng. Struct.* **2017**, *145*, 190–210. [CrossRef]
42. Siano, R.; Roca, P.; Camata, G.; Pelà, L.; Sepe, V.; Spacone, E.; Petracca, M. Numerical investigation of non-linear equivalent-frame models for regular masonry walls. *Eng. Struct.* **2018**, *173*, 512–529. [CrossRef]
43. Siano, R.; Camata, G.; Sepe, V.; Spacone, E.; Roca, P.; Pelà, L. Numerical validation of equivalent-frame models for URM walls. In Proceedings of the ECCOMAS Congress 2016—VII European Congress on Computational Methods in Applied Sciences and Engineering, Crete Island, Greece, 5–10 June 2016; Institute of Structural Analysis and Antiseismic Research School of Civil Engineering—National Technical University of Athens (NTUA): Crete Island, Greece, 2016; Volume III, pp. 5262–5273, ISBN 978-618-82844-0-1. [CrossRef]
44. Sepe, V.; Spacone, E.; Raka, E.; Camata, G. Seismic analysis of masonry buildings: Equivalent frame approach with fiber beam elements. In Proceedings of the 9th International Conference on Structural Dynamics, Porto, Portugal, 30 June–2 July 2014; pp. 237–244.